Systematically quantifying oil–water microemulsion structures using (spin-echo) small angle neutron scattering

Mulder, Maarten; Li, Xuesong X.; Nazim, Mohammad M.; Dalgliesh, Robert M.; Tian, Bei; Buijse, Marten; van Wunnik, John; Bouwman, Wim G.

DOI
10.1016/j.colsurfa.2019.04.045

Publication date
2019

Document Version
Final published version

Published in
Colloids and Surfaces A: Physicochemical and Engineering Aspects

Colloids and Surfaces A 575 (2019) 166–175

Contents lists available at ScienceDirect

Colloids and Surfaces A

journal homepage: www.elsevier.com/locate/colsurfa

Systematically quantifying oil–water microemulsion structures using (spin-echo) small angle neutron scattering

Maarten Mulder[a], Xuesong X. Li[b], Mohammad M. Nazim[a], Robert M. Dalgliesh[c], Bei Tian[a], Marten Buijse[b], John van Wunnik[b], Wim G. Bouwman[a,*]

[a] Faculty of Applied Sciences, Delft University of Technology, Delft, Netherlands
[b] Shell Global Solutions B.V., Rijswijk, Netherlands
[c] ISIS, Rutherford Appleton Laboratory, STFC, Didcot, United Kingdom

GRAPHICAL ABSTRACT

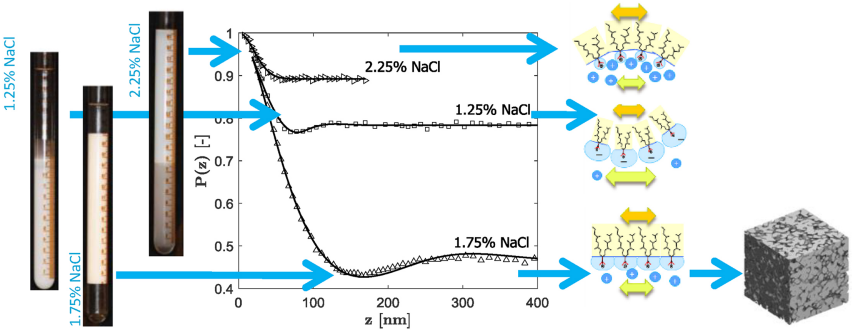

ABSTRACT

Microemulsion systems consisting of D_2O, an alkane, an anionic internal olefin sulfonate surfactant, salt and secondary butyl alcohol (SBA) as co-solvent are studied in a systematic way. In four different sample sets, either the salt content, SBA content or alkane carbon number was varied in order to study the effects of the individual compounds on the structure sizes making up the microemulsion. Using complementary small-angle neutron scattering techniques SANS and Spin-Echo SANS, it was found that the microemulsion systems exhibit the largest structures in the optimum state (domain size of $d/2 = 144$ nm in the model by Teubner and Strey), where the structure is considered bicontinuous. In comparison, at under- and over-optimum states where the structures consist of emulsified spherical droplets, the smallest measured diameter was $2R = 44$ nm. Furthermore, the structure sizes in bicontinuous microemulsions decrease exponentially (down to $d/2 = 15$ nm for pentadecane and 5 wt% SBA) as function of both SBA content and alkane carbon number. The observed trends in structure sizes combined with the trends observed in the area per surfactant molecule, are qualitatively explained with the extended Winsor R-ratio, the HLD-NAC model and surfactant film flexibility arguments.

1. Introduction

Microemulsions are isotropic, thermodynamically stable dispersions consisting of water, oil and one or more types of surfactants, in which the formed structures are in the order of 10^0–10^2 nm in size [1]. These systems are incredibly versatile, and are studied in a wide variety of research areas such as drug delivery [2], enhanced oil recovery (EOR) [3,4], the potential use of supercritical CO_2 as a sustainable solvent [5], and one can find commercial applications in toiletries, cosmetics, paints and many more [6,7]. Depending on the application, one of the many

* Corresponding author.
E-mail address: w.g.bouwman@tudelft.nl (W.G. Bouwman).

https://doi.org/10.1016/j.colsurfa.2019.04.045
Received 4 April 2018; Received in revised form 11 April 2019; Accepted 16 April 2019
Available online 26 April 2019

characteristics of microemulsions can be of interest and can be measured with a variety of instruments. One of these characteristics, for example, is the interfacial tension which is the work required for a two-phase system to create more interfacial area, and can be measured with a spinning-drop tensiometer [8]. Furthermore, the structures and structure sizes of microemulsions can be measured with dynamic light scattering (DLS) [9], fluorescence correlation spectroscopy (FCS) [10], small angle X-ray scattering (SAXS) [11], small angle neutron scattering (SANS) [12] and spin-echo SANS (SESANS), of which the latter two are used in this work. The determination of self-diffusion coefficients can be achieved with nuclear magnetic resonance (NMR) [13], or when information about the viscosity of microemulsions is required, conventional rheology can be applied. Additionally, all of these characteristics are generally dependent on temperature and pressure.

In the field of chemical EOR, surfactant solution is injected into the oil reservoir to reduce the interfacial tension between the oil phase and the aqueous phase, to an ultra-low value, in the order of 0.001 mN/m, to mobilize the capillary trapped oil in the rock pores. This process improves the solubilization and therefore the mobility of the oil significantly.

In general, for a target chemical EOR application case, the geochemical character such as the reservoir rock mineralogy, the aqueous and oil phase composition, the temperature and pressure ranges are the known conditions. The screening condition for the surfactant and co-solvent are low adsorption on the rock surface, good brine tolerance and suitable solubility, good temperature stability, and good mobility, for instance no larger structures like gels or crystal being formed. At the same time, the oil recovery efficiency by using the surfactant is always pre-investigated on a rock sample, the so-called core-flooding experiment. Unfortunately, the number of surfactant which is economical and also meet all these criteria is not plentiful, Negin et al. [14] summarized a list of most commonly used surfactants for chemical EOR. From these the anionic surfactant is the preferred choice for sandstone reservoir. Bera et al. [3] in their review article pointed out that microemulsion structure has a key role in the applied fields.

For a high temperature reservoir, above 80 °C, internal olefin sulfonate (IOS) which is stable up to 120 °C is one of the preferred surfactants. However, due to the poor solubility of it in brine and low oil recovery efficiency when using it alone, a co-solvent, such as secondary butanol alcohol (SBA) is always added to the system [15]. In such a quarterly system (oil, brine, surfactant, co-solvent), carefully tuning the salinity, the concentration of the surfactant and co-solvent, an low IFT a (Winsor type III) microemulsion will be formed [16].

However, in the oil reservoir, stable microemulsions can sometimes form, which have the disadvantage that the viscosity of this phase is generally much higher than the surrounding phases [17], increasing the difficulty of oil production. As a consequence, many (viscosity) experiments are carried out in this research field to characterize large sets of samples consisting of water-salt-oil-surfactant with a variety of compositions, to find the best formulation for particular types of rock and oil from oil reservoirs.

In such a study by Humphry et al. [18] the viscosity of microemulsion systems was measured, both with conventional rheology and core-flooding experiments. The latter technique provides values closer to the in-situ viscosity, in which the microemulsion phase flows through a sample of rock retrieved from the (potential) drilling site in question. They found that the apparent viscosity can be several times higher in comparison to the values obtained with conventional rheology measurements. In an attempt to explain this discrepancy, the pore throat size distribution of a representative rock reservoir sample was measured, as is shown in Fig. 1.

It is hypothesized in this paper that the sizes of the structures of the microemulsions that form are in the same order of magnitude as the smallest 10% of the pore throats. As a consequence, this requires a higher local pressure gradient to be applied in order for the microemulsion to flow through the rock formation, which in core-flooding

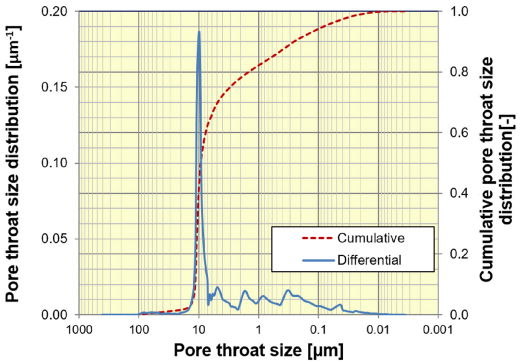

Fig. 1. Differential intrusion plot, showing the pore throat size distribution (drawn curve) and the cumulative distribution (dashed curve) for a representative rock sample. This shows that 10% of the pore throats are smaller than 300 nm in size.

experiments results in a higher measured viscosity. It also found by Sahni et al. [19] and Chang et al. [20] that the additional co-solvent significantly can reduce the apparent viscosity of the mixture, from which we theorized that co-solvent reduces the structure size in the microemulsion.

To confirm this possible explanation, a large set of microemulsions with varying compositions, similar to the samples studied by Humphry et al., is studied in this work. The goal is to identify the structure and structure sizes making up the microemulsion phase, with the main focus on quantifying the effects of the variation of alkane carbon number, co-solvent content and salt content. To this end, small angle neutron scattering measuring techniques are applied, mainly because of their capability of probing nanoscale structures, but also because they indirectly provide information about the sharpness of the oil/water interface and the interfacial area occupied per individual surfactant molecule. Based on a preliminary study it was decided to make use of both SANS and SESANS techniques. The structure sizes can vary significantly per microemulsion composition and potentially exceed the limited range of 1–100 nm of conventional SANS. Therefore, including SESANS with its wide range 30 nm up to 20 µm, the two techniques provide the opportunity to scan the full size range. For sufficiently a large sample size, one is then able to create models to predict behaviour of microemulsions making use of the theory of e.g. hydrophilic lipophilic deviation-net average curvature (HLD-NAC) [21,22]. This semi-empirical method allows for the modeling of combinations of microemulsion systems, making the extension towards complicated, more realistic systems easier. However, this is beyond the scope of this current paper.

2. Experimental

2.1. Materials

Sodium chloride (NaCl), deuterated water (D_2O), *n*-decane ($C_{10}H_{22}$), *n*-dodecane ($C_{12}H_{26}$), *n*-pentadecane ($C_{15}H_{32}$), secondary butyl alcohol (C_4H_9OH) were purchased from Sigma-Aldrich, and internal olefin sulfonate (IOS) surfactant ENORDET™ O242 ($C_{20-24}H_{39-47}SO_3Na$) were purchased from Shell Chemicals (Netherlands). The IOS surfactant as bought comes solved in H_2O with an active weight percentage of 36.6%, and has an average molecular weight of 410 g/mol. The compounds were not further purified.

2.2. Samples

The microemulsions in this study are quinary systems consisting of D_2O, secondary butyl alcohol (SBA), sodium chloride, one of three aforementioned alkanes, and an IOS surfactant. This surfactant has two hydrophobic tails and a hydrophilic anionic head group, and is

Table 1
Overview of the composition of the samples measured in this study. The water phase of each sample consists of D_2O, and contains, in addition to the compounds listed below, 2 wt% of IOS surfactant. The percentages are relative to the water solution, as is described in the text. Note that sample A1 occurs twice.

Sample no.	Oil phase	SBA [wt%]	NaCl [wt%]	ϕ_o	ϕ_w	Winsor type
A1	Decane	1.0	1.50	0.22	0.78	WI/WIII
A2	Decane	3.0	1.50	0.31	0.69	WIII
A3	Decane	5.0	1.50	0.38	0.62	WIII
B1	Decane	1.0	1.00	0.06	0.94	WI
B2	Decane	1.0	1.25	0.14	0.86	WI
A1	Decane	1.0	1.50	0.22	0.78	WI/WIII
B3	Decane	1.0	1.75	0.51	0.49	WIII
B4	Decane	1.0	2.00	0.79	0.21	WII
B5	Decane	1.0	2.25	0.82	0.18	WII
C1	Dodecane	1.0	2.50	0.58	0.42	WIII
C2	Dodecane	3.0	2.50	0.55	0.45	WIII
C3	Dodecane	5.0	2.50	0.57	0.43	WIII
D1	Pentadecane	1.0	4.20	0.36	0.64	WIII
D2	Pentadecane	3.0	4.20	0.25	0.75	WIII
D3	Pentadecane	5.0	4.20	0.20	0.80	WIII

therefore sensitive to the salt content (salinity) in the water phase. SBA is a medium chain alcohol and acts as co-solvent.

The samples are prepared by dissolving the IOS surfactant, SBA and sodium chloride in D_2O in the desired ratios, after which an equal volume of alkane is added to the mixture. In Table 1 an overview of all studied samples is given, in which the weight percentages are relative to the total weight of the D_2O and SBA solution. The volume fractions ϕ_o and ϕ_w for oil and water, respectively, in the microemulsion phase are given as determined from phase behaviour analysis and have an uncertainty of 0.05 ml. Indicated additionally is the Winsor type [23] of the system, which classifies an oil-in-water microemulsion as Winsor type I (WI), a water-in-oil microemulsion as Winsor type II (WII) and a bicontinuous microemulsion as Winsor type III (WIII). The determination of the Winsor type is based on the phase behaviour of the samples, of which photographs are given in the Supporting information. Following Winsor scheme, the phase behavior of ionic surfactant (in this study) system is a function of salinity [24]. At low salinity the system is Winsor I and when salinity increases it goes through the transition I → III → II. In this transition, the IFT between the oil and water phase is first reducing and then increasing, within type III, the desired ultra-low IFT for EOR application is reached. For this reason, most of the samples analyzed in this paper have a Winsor III type phase behaviour. The samples are divided into four sets, where in set A, C and D the SBA content is varied for decane, dodecane and pentadecane, respectively. In set B the salinity is varied for decane only. Furthermore, all samples have a constant surfactant active weight percentage of 2%. This surfactant concentration is relatively low and is away from the phase inversion salinity, which is at least above 5%, in a Kahlweit fish type phase diagram. More details about the sample preparation procedure can be found in the Supporting Information.

2.3. Methods

2.3.1. SANS

Small angle neutron scattering measurements were performed with the LARMOR instrument in the ISIS facility, located at the Rutherford Appleton Laboratory (Didcot, United Kingdom). LARMOR is a time-of-flight SANS instrument using neutrons with wavelengths ranging from $0.9 < \lambda < 13.3$ Å. The measured quantity is the intensity $I(Q)$ [cm^{-1}] as function of the wave vector transfer Q [$Å^{-1}$], given by

$$Q = \frac{4\pi}{\lambda}\sin\left(\frac{\theta}{2}\right) \tag{1}$$

with θ the scattering angle. Combined with the physical specifications of the LARMOR setup this allowed for a Q-range of $0.006 < Q < 0.489\ Å^{-1}$. All samples were measured in 1 mm path length quartz cuvettes at room temperature ($T_R \approx 298$ K). The crude data were masked, radially averaged and scaled according to standard procedures of the facility. The incoherent background was subtracted by a linear combination of the contributions from D_2O and the alkane, according to the volume fractions in the microemulsions measured visually during phase behaviour analysis. The presence of the other compounds gives an uncertainty in the background subtraction of $3 \times 10^{-1}\ cm^{-1}$.

2.3.2. SESANS

The spin-echo small angle neutron scattering measurements were carried out at the SESANS setup located at the Reactor Institute Delft [25], part of the Delft University of Technology (Netherlands). This setup utilizes monochromatic neutrons with a wavelength of $\lambda = 2.03$ Å($\Delta\lambda/\lambda = 5\%$). The samples were measured at room temperature in quartz cuvettes with a path length of 2 mm. For some samples a path length of 4 mm was created by placing two 2 mm path length cuvettes in succession, to improve the amount of scattering in favour of the quality of the measured signal.

SESANS yields the dimensionless polarization $P(z)$ of the transmitted neutrons, as function of the spin-echo length z [nm],

$$P(z) = e^{\lambda^2 t(G(z)-G(0))} \tag{2}$$

with t the neutron path length through the sample and $G(z)$ the projection of the autocorrelation of the density distribution function of the sample. $G(z)$ is directly related to the intensity function $I(Q)$ from a SANS experiment [26],

$$G(z) = \frac{1}{2\pi}\int_0^\infty J_0(Qz)I(Q)QdQ \tag{3}$$

where J_0 is the zeroth order Bessel function of the first kind. This enables the extensive catalogue of models available from the SANS community to be used directly for SESANS data analysis. For some simple shapes, such as spheres and spherical shells, analytical expressions for $G(z)$ have been derived of which an overview is given by Andersson et al.

2.3.3. Models

In sample sets A, C and D the microemulsions are in the optimum states (Winsor type III), where the structure can expected to be bicontinuous [27]. Teubner and Strey developed a phenomenological model for these systems [28], which has proven to accurately describe the scattering peak in SANS experiments for a wide variety of systems [29,11,12,30,31]. There are additional approaches available to model bicontinuous microemulsions. For example, a Clipped Random Wave model with an inverse 8th-order polynomial spectral density function yields, in addition to the relevant length scales, information about the curvature of the interface [32,33], and with the generalised indirect Fourier transform (GIFT) method one obtains a pair distribution function [34]. However, the model by Teubner and Strey is by far the most simple and least computationally intensive approach, and therefore only this model has been used in this work.

Teubner and Strey postulated an expression for the autocorrelation function $\gamma_{TS}(r)$ of the density distribution,

$$\gamma_{TS}(r) = \frac{d}{2\pi r}\sin\left(\frac{2\pi r}{d}\right)e^{-r/\xi_{TS}} \tag{4}$$

where d is the mean domain repetition length and ξ_{TS} the correlation length of the system. The expression for $I_{TS}(Q)$ for SANS experiments can then be obtained by a Fourier transform, resulting in

$$I_{TS}(Q) = \frac{1}{\xi_{TS}}\frac{8\pi\phi_w\phi_o\Delta\rho^2}{Q^4 - 2\left(\left(\frac{2\pi}{d}\right)^2 - \left(\frac{1}{\xi_{TS}^2}\right)\right)Q^2 + \left(\left(\frac{2\pi}{d}\right)^2 + \left(\frac{1}{\xi_{TS}^2}\right)\right)^2} \tag{5}$$

where has been multiplied with $\phi_w\phi_o\Delta\rho^2$ to get to absolute units of [cm^{-1}], in which Δρ is the scattering length density contrast. For SESANS an expression for $G(z)$ is needed but has not been derived up to now. Using the integral for the projection of the autocorrelation function $\gamma_{TS}(r)$ as given by Andersson et al., the result for $G_{TS}(z) - G_{TS}(0)$ is given by

$$G_{\mathrm{TS}}(z) - G_{\mathrm{TS}}(0) = \phi_o\phi_w\Delta\rho^2\frac{d}{2\pi}\left[\mathrm{i}[K_0(\mathrm{bz}) - K_0(-\mathrm{az})] - \left[2\arctan\left(\frac{2\pi\xi_{\mathrm{TS}}}{d}\right)\right]\right] \quad (6)$$

where i is the imaginary unit, $K_0(z)$ is the zeroth order modified Bessel function of the second kind, and a and b are constants dependent on d and ξ_{TS}. The definitions for a and b and the complete derivation for $G_{TS}(z)$ are given in Appendix A. Note that despite the imaginary prefactor, $G_{TS}(z)$ is a real function.

In sample set B the salinity is scanned, where the microemulsion structures transition from droplets (under-optimum) to bicontinuous (optimum) to droplets (over-optimum). Assuming a dilute system of spherical droplets, a lengthy analytical expression for $G(z)$ is available [35], but the simpler approximation by Andersson et al. works equally well,

$$G(z) \approx \phi\Delta\rho^2 e^{-9/8(z/R)^2} \quad (7)$$

where is multiplied with $\phi\Delta\rho^2$ to obtain absolute units, in which ϕ is the volume fraction corresponding to the emulsified droplets. R denotes the radius of the spherical droplet. However, while varying the salinity, at some point the droplets will grow in size and the system can therefore not be considered a dilute solution anymore. At this point the systems behaves more like a hard spheres liquid. There exists no analytical expression for $G(z)$ for this kind of system, and Eq. (3) has to be used in combination with the form factor for spheres, and the structure factor for hard spheres based on the Percus-Yevick approximation [36].

Model fitting for both SANS and SESANS data has been done with SasView 4.1, in which support for the latter technique has been added [37].

3. Results and discussion

This section is divided into three subsections where the salinity scan (sample set B), SBA scan and carbon number scan (sample sets A, C, D) will be discussed separately.

3.1. Salinity scan

Sample set B consists of 6 samples where the salinity is varied from 1.00 wt% to 2.25 wt%, while the weight percentages of the other compounds are kept constant. As is given in Table 1, from studying phase behaviour it was observed that the microemulsions transitioned from Winsor Type I→III→II. The SESANS measurements for this sample set are given in Fig. 3, in which the corresponding sample numbers and salinities are indicated.

As a common practice in EOR surfactant investigation, the Winsor type phase behaviour of these combinations are pre-screened with varying salinity. The phase behavior is analyzed by plotting the oil and brine solubilization curves. The oil and brine solubilization are defined as below,

$$\sigma_o = V_{\mathrm{oil,me}}/V_{\mathrm{surf}} \quad (8)$$

and

$$\sigma_w = V_{\mathrm{wat,me}}/V_{\mathrm{surf}} \quad (9)$$

with $V_{\mathrm{oil,me}}$ and $V_{\mathrm{wat,me}}$ the oil and brine volumes in the microemulsion and V_{surf} the total surfactant volume in the system. See Fig. 2, a solubilization plot of the system with decane, for the formulations (see Table 1). At the optimum salinity (about 1.7% NaCl) the oil and brine solubilization in the microemulsion are equal and the IFT will be at a minimum. The surfactant/co-solvent formulations studied in this paper are all close to the optimum salinity at which the IFT reaches its lowest value.

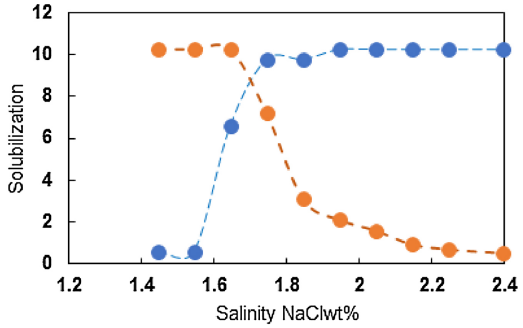

Fig. 2. Oil and brine solubilization in the microemulsion as a function of salinity.

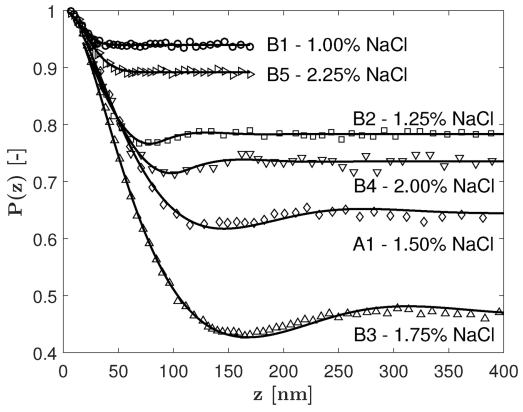

Fig. 3. SESANS measurements on all samples in the salinity scan. The difference between dilute spherical droplets (B1, B5) and concentrated droplets with a hard sphere interaction (B2, B4) is evident. Sample A1 can be described as either a bicontinuous phase or containing hard spheres (see text), whereas Sample B3 is in the bicontinuous phase. The error bars are equal or smaller than the size of the icons in the figure.

The continuous curves in Fig. 3 are obtained from fitting, and the corresponding obtained structure size parameters are given in Table 2, where for each sample is indicated which model has been used to fit the data to. It is clear that for the dilute systems of samples B1 and B5 the emulsified droplets are the smallest in size. For the more concentrated systems of samples B2 and B4, the droplets have larger radii. Additionally, a hard sphere interaction emerges as a local maximum in the curves, of which the corresponding spin-echo length z represents the average distance between two droplets. As will be discussed below, for sample A1 both the hard sphere and Teubner–Strey model yielded good fits. Lastly, sample B3 is a typical WIII microemulsion and consists of the largest structures of this sample set.

Furthermore, Porod's law [38] was applied on the SANS data where possible, from which the total specific surface area of a system with a sharp interface is obtained, independent of the aforementioned models. From this information the occupied area per surfactant molecule A_s can then be calculated. However, for the samples in set B no obvious trend for A_s is observed.

As Krouglov et al. [35] demonstrated, dilute spherical particles can be easily distinguished from a concentrated system of spheres with hard sphere interactions with SESANS. In Fig. 3 this same distinction can be made between sample B1 (dilute spheres, 1.00 wt% NaCl) and sample

Table 2
Results for the size parameters from fitting the data to the Teubner–Strey (TS) model, dilute spheres form factor (DS) or the DS form factor with the hard sphere structure factor included (HS). It is indicated per sample from which technique the values were obtained. The area per surfactant molecule A_s is also given, which are calculated from SANS data.

Sample	Model	Δρ [10^{-6} Å^{-2}][a]	[d] [nm]	ξ_{TS} [nm]	R [nm]	A_s [Å^2]	Technique
A1	TS, HS	5.7 ± 0.2	251 ± 2	98 ± 3	82 ± 1	26 ± 2[d]	SESANS
A2	TS	4.7 ± 0.2	105 ± 3	37 ± 3	–	80 ± 5	SESANS
A3[b]	TS	6.4 ± 0.2	39 ± 1	18 ± 1	–	87 ± 6	SANS
B1	DS	4.4 ± 0.2	–	–	22 ± 1	72 ± 5	SESANS
B2	HS	6.6 ± 0.2	–	–	46.0 ± 0.4	84 ± 5	SESANS
A1	TS, HS	5.7 ± 0.2	251 ± 2	98 ± 3	82 ± 1	26 ± 2	SESANS
B3	TS	5.7 ± 0.2	287 ± 1	132 ± 2	–	69 ± 4	SESANS
B4	HS	5.7 ± 0.2	–	–	65 ± 1	–	SESANS
B5	DS	4.1 ± 0.2	–	–	31 ± 1	69 ± 4	SESANS
C1	TS	4.1 ± 0.2	156 ± 1	89 ± 4	–	58 ± 4	SESANS
C2[b]	TS	6.7 ± 0.2	52 ± 1	22 ± 1	–	69 ± 4	SANS
C3[b]	TS	5.9 ± 0.2	29 ± 1	11 ± 1	–	73 ± 5	SANS
D1[c]	–		–	–	–	–	–
D2[b]	TS	7.0 ± 0.2	30 ± 1	14 ± 1	–	63 ± 4	SANS
D3[b]	TS	7.4 ± 0.2	19 ± 1	7 ± 1	–	83 ± 6	SANS

[a] All Δρ values are obtained from fitting. The trends within sample sets are not further discussed, but some insight is given in the Supporting Information.
[b] Values obtained from fitting including the incorporation of multiple scattering effects as calculated by Schelten and Schmatz. The error is estimated.
[c] Sample D1 did not produce any consistent results, likely due to the large number of phases (> 3) present thus not being a well-defined 3 phase microemulsion.
[d] For the calculation of A_s is assumed that all the surfactant molecules are located on the oil/water interface within the microemulsion phase. For sample A1 this assumption is not correct and surfactant molecules are located in the bottom phase as well. As a result too many surfactant molecules are allocated to the interface and the calculated value of A_s is too low.

B2 (concentrated spheres, 1.25 wt% NaCl). This transition can be illustrated with the (extended) Winsor R-Ratio [39] (here denoted as R_W), describing the ratio of the net cohesive interaction energies between the surfactant and the oil phase, and the surfactant and the water phase. The Winsor R-theory is conceptually attractive to explain microemulsion properties. For a more rigorous discussion of the physics of the oil/surfactant/water interface, within the context of microemulsions, see the recent paper by Fraaije et al. [40]. The R-ratio is given by

$$R_W = \frac{A_{SO} - A_{OO} - A_{LL}}{A_{SW} - A_{WW} - A_{HH}}, \tag{10}$$

where $A_{\alpha\beta}$ is the energy associated with the interaction between entity α and β, where O and W represent oil and water, respectively, S is the surfactant and L,H are the surfactant tails and head groups, respectively. A WI (WII) microemulsion corresponds to $R_W < 1$ ($R_W > 1$), and a WIII microemulsion results in $R_W = 1$. An R_W value of 1 means that the net interactions on the oil and water side of the interface are in balance, and therefore the interface tends to be flat. It is further speculated that the net values of numerator and denominator are a measure for the stiffness or flexibility of the interface film. Note that A_{HH} is negative due to the negatively charged heads of the IOS surfactant molecules repelling each other [41]. In addition it is assumed that A_{LL} is also negative due to the bulky, spread-out double tails of the surfactant repelling each other, resulting in a similar effect as the repulsion among the charged head groups. Osmotic pressure build-up by the oil molecules migrating in between the surfactant tails is another mechanism for spreading out of the surfactant molecules. This mechanism is here assumed to be covered by part of the energy term A_{SO}. The larger the oil molecules the smaller the osmotic contribution to A_{SO}.

Although for both sample B1 and B2 holds that $R_W < 1$, sample B2 has a higher salinity than B1. This implies that more positively charged sodium ions are present which reduce the effective repulsion of the negatively charged heads of the surfactant molecules. In other words, from B1→B2 the interaction energy A_{HH} is lowered (becomes less negative), and thus the R-ratio increases towards $R = 1$. This results in a decrease of the curvature of the interface, implying bigger droplets. This explanation agrees with the observation of the increase in radius, where for sample B2 the radius is more than double the radius of sample B1.

Unlike distinguishing dilute and hard sphere systems in SESANS measurements, the distinction between hard spheres and bicontinuous structures is hard to make due to the similarity in the correlation function of both systems, producing a similar oscillation-like SESANS curve. Therefore for samples B2-B4 and A1, in each case both models have been fitted to the data. Based on the quality of each fit in combination with observations of phase behaviour, it was concluded which model was the most likely to represent the structure of the sample. The results from this procedure not present in Table 2 are given in the Supporting Information.

Although for samples B1–5 it was obvious with which Winsor type they could be described, for sample A1 it was not clear. A middle phase was present, which implies a microemulsion of the type WIII. However, the boundary between the bottom and middle phase was diffuse, making the distinction between the bottom and middle phase harder to make, implying a WI microemulsion. Due to the long equilibrium times, as described in the Supporting Information, it is possible that sample A1 had not fully equilibrated yet. However, while increasing the salinity in a salinity scan, at some point the droplets grow in size, such that they eventually coalesce and form continuous domains leading to the bicontinuous structure [7]. This switch in structure is not instantaneous, but a continuous transition. This could explain that both the hard sphere and Teubner–Strey model fit the data equally well, producing realistic values for R and d, ξ_{TS}, respectively.

Sample B3 is at optimum salinity with equal amounts of oil and water emulsified in the middle microemulsion phase, typical for a WIII microemulsion. The net interaction energies in the numerator and denominator of Eq. (10) are now exactly equal ($R_W = 1$) because the repulsive forces on either side of the oil/water interface are balanced. The curvature of the interface is therefore zero on average, producing the bicontinuous structure.

Increasing the salinity from this point reduces the repulsion among the surfactant head groups even further (A_{HH} becomes less negative, approaching zero), such that the swelling forces of the hydrophobic tails dominate, resulting in a nonzero curvature. This creates spherical droplets of water emulsified in oil, where now holds that $R_W > 1$. The transition thus continues from a bicontinuous to a hard sphere system (Sample B4, 2.00 wt% NaCl) and eventually to a dilute system of water droplets (Sample B5, 2.25 wt% NaCl), producing the characteristic SESANS curves similar to the curves from samples B2 and B1,

respectively. As was observed for samples B1 and B2, due to the smaller curvature, the radius of sample B4 is similarly more than double than the radius of sample B5.

Although particulate microemulsion systems are known to be polydisperse [42,43], this is not taken into account in the results in Table 2. As Uca et al. [44] demonstrate, SESANS is not sensitive to small polydispersities. For example, a dilute monodisperse system with a droplet radius of $R = 100$ nm and a polydisperse system with a mean radius of $R = 80$ nm and a Full-Width Half-Max of 20 nm yield similar curves because in both cases correlations disappear at $2R_{(max)} = 200$ nm. Therefore, the fit results should be interpreted as maximum droplet radii. However, the effect of polydispersity is more pronounced in concentrated systems with hard sphere interactions, and for sample A1, B3 and B4, estimates are given in the Supporting Information.

Regardless of the exact distribution of radii per sample, the obtained structure sizes are on the same length scale as the smallest 10% of the pore throat size distribution in Fig. 1. Especially the type WIII microemulsion of sample B3 with the desired ultra-low interfacial tension, has a domain repetition length of nearly 300 nm which is larger than the size of a significant part of the pore throats present. Additionally, preliminary studies by the authors on in-situ SANS measurements on similar samples put under shear in a rheometer, indicate that structures tend to increase in the direction of shear, of which indicative figures are given in the Supporting Information. Altogether these are indications that due to the sizes of the bicontinuous structures, the microemulsion phase might have difficulty flowing through the porous rock. The required increase in the pressure applied in core-flooding experiments, results then in a higher apparent viscosity. The statement 'difficulty of flowing' intrinsically assumes that the stiffness or deformability of the surfactant film does not change when the size or curvature of the interface is changed. For size changes due to salinity changes (salinity scan) this is likely to be the case. In contrast, when sizes are changed due to changes in the SBA content this is likely incorrect, and interfaces might change their degree of flexibility and consequently their resistance to deformation when squeezed through pore necks.

3.2. SBA scans

Sample sets A, C ad D consist of 3 samples each, where the SBA content is varied from 1 wt% to 5 wt%, while the weight percentages of the other compounds are kept constant. Although all samples except A1 are type WIII microemulsions, the volume fractions ϕ_o and ϕ_w as given in Table 1 are not constant in set A and D. The effect of the co-solvent on the phase behaviour can be clearly observed during the phase behaviour test, as shown in the photograph in the supplementary material of this paper in Fig. 5.

In Fig. 4 the SANS data (samples C2 and C3, left panel) and SESANS data (samples C1 and C2, right panel) are shown for sample set C as an example, and similar figures for the sample sets A and D are given in the Supporting Information. It differs per sample whether SANS or SESANS is the most sensitive technique, due to the large range in structure sizes of the samples. The results in Table 2 are obtained from the most sensitive technique, which is indicated in the table for each sample. Due to the presence of multiple scattering effects in the SANS measurements, only data from singly scattered neutrons are given in Fig. 4 and therefore no regular fitted curve is shown. In the data analysis of SANS measurements, the multiple scattering effects have been taken into account with the treatment proposed by Schelten and Schmatz [45]. However, their formalism assumes a monochromatic neutron beam, and therefore additional steps have to be taken due to the time-of-flight nature of the LARMOR instrument. A full description of the fitting process and additional figures are given in the Supporting Information.

Note that in the right panel of Fig. 4 no fitted curve is shown for the measurement on sample C2, because neither the hard sphere nor the Teubner–Strey model fitted properly. However, the data of sample C2 shows a local maximum at a spin-echo length of $z \approx 50$ nm, matching the result of $d = 52$ nm obtained from SANS. In the left panel of Fig. 5 the Teubner–Strey parameter d is plotted as function of the SBA content for all samples in sets A, C and D, with the vertical axis on a logarithmic scale. An exponential decrease in d with increasing SBA content is evident for each sample set.

Additionally, in the right panel of Fig. 5 the area per surfactant molecule A_s is plotted as function of SBA content. An increase in A_s is observed for each sample set as the SBA content increases.

Interestingly, the size of the oil and water domains decrease (d, ξ_{TS}) with increasing SBA content, while the area covered by a surfactant molecule on the oil water interface increases. The explanation being, that part of the SBA molecules reside on the interface, take up space and tend to push the surfactant molecules farther apart. This creates more physical space on the interface (see parameter A_s in Table 2 and Fig. 5) in which the surfactant molecules can move about, possibly, resulting in a more flexible interface. These flexible interfaces could fold more easily and despite the larger A_s the domain sizes still can decrease with increasing SBA content.

Further inspection of Table 1 shows for set A (decane) an increase in the volume fraction ϕ_o with increasing SBA content, for set C (dodecane) ϕ_o stays approximately constant and set D (pentadecane) shows a decrease in ϕ_o. Before seeking an explanation for this behaviour it is worth noting that the sets A, C and D are not all in the same location within the Windsor III range. Set A is somewhat under-optimum as $\phi_o < \phi_w$, set C is slightly over-optimum and so $\phi_o \phi_w$ and set D again is somewhat under-optimum. To better understand the opposing ϕ_o dependencies on SBA content, use is made of the HLD-NAC model [46]. A principle outcome of the HLD-NAC model is the water and oil domain size in micro-emulsions. According to the NAC theory, the relation between the oil and water domain radii (R_o and R_w, respectively. Note that there is a distinction to be made between R_w and R_W, the latter being the Winsor R-ratio) is given by

$$\frac{1}{R_o} - \frac{1}{R_w} = -\frac{\mathrm{HLD}}{L} \tag{11}$$

where L is a characteristic surfactant molecule length and where HLD is given by e.g. salinity, temperature, type of surfactant molecule and effective alkane number of the oil. However, the amount of added co-solvent such as SBA will also impact HLD and our acquired values of the

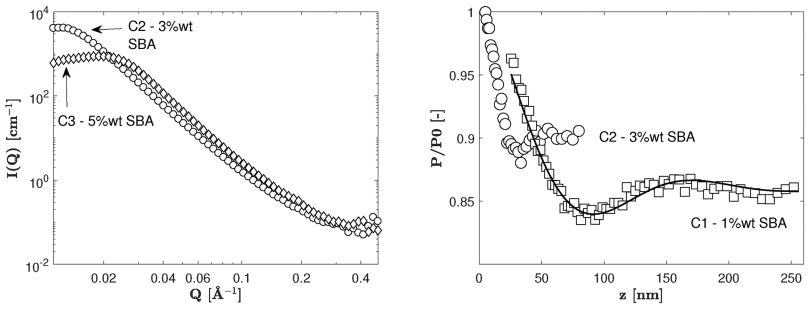

Fig. 4. SANS data (left), and SESANS data (right) for samples C1 (□), C2 (○) and C3 (♦). The error bars are equal or smaller than the size of the icons in the figure. The continuous curve for sample C1 is obtained from the model fitting with the Teubner–Strey model. The reason of absence of fitted curves for the other samples is explained in the text.

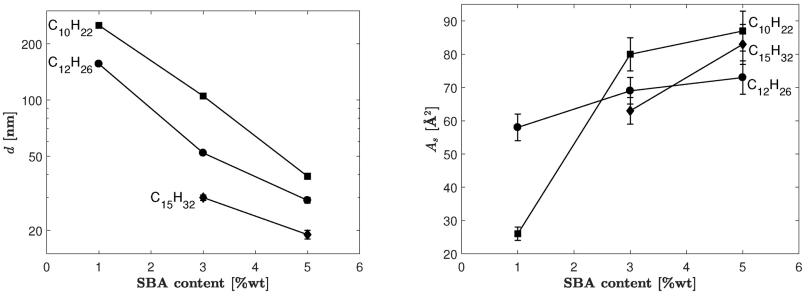

Fig. 5. Teubner–Strey parameter d in nm (left panel, semi-logarithmic scale) and the area per surfactant molecule A_s in Å^2 (right panel), each as function of SBA content in wt%, for decane (■, set A), dodecane (•, set C) and pentadecane (◆, set D). The lines are a guide to the eye. Error bars are given in both figures.

Table 3
Calculated values relevant to the HLD-NAC theory. In these calculations, the measured values for d are considered the typical domain sizes for oil ($d_o = 2R_o$). From this, d_w and therefore R_w can be calculated.

Sample	SBA [wt%]	ϕ_o	d [nm]	R_o/R_w	d_w [nm]	L/HLD	L/HLD norm.
A1	1.0	0.22	251	0.66	383	−365	1.63
A2	3.0	0.31	105	0.77	137	−224	1.00
A3	5.0	0.38	39	0.85	46	−130	0.58
C1	1.0	0.58	156	1.11	140	−687	1.83
C2	3.0	0.55	52	1.07	49	−376	1.00
C3	5.0	0.57	29	1.10	26	−147	0.39
D1	1.0	0.36		0.83			
D2	3.0	0.25	30	0.69	43	−49	1.00
D3	5.0	0.20	19	0.69	30	−26	0.52

oil and water domain radii give the opportunity to reveal the dependence of HLD on SBA content.

To apply the HLD-NAC model, first Tables 1 and 2 have been combined into Table 3. In addition, a column has been added in which the effective value of the ratio of the oil and water domain sizes from ϕ_o is estimated, by assuming spherical oil and water droplets, i.e. $R_o/R_w = \sqrt[3]{\phi_o/\phi_w}$. Additionally, the value of water domain sizes have been estimated by using this ratio and the value of d together. Lastly, the inverse of HLD/L (L/HLD) are calculated and given as this proves to show a good correlation with the SBA content, and are shown together with the normalized value of L/HLD per oil type with respect to the value of L/HLD at an SBA content of 3%.

To emphasize the linear behaviour of the L/HLD parameter, the values are plotted in Fig. 6 for sample sets A, C and D. The figure shows a good correlation between the normalized L/HLD values and the SBA content. Increasing the SBA content from 1 wt% to 5 wt% decreases the L/HLD value with approximately a factor 3.5. The factor is the same for the three tested oil types. Additionally, the salinities, which are around the optimum salinities, are not impacting it. The earlier observed opposing trends of ϕ_o with changing SBA content for the different oils, are

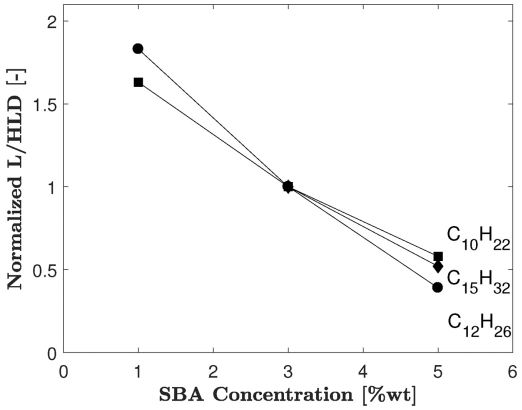

Fig. 6. Normalized L/HLD values as function of SBA content [wt%], for decane (■, set A), dodecane (•, set C) and pentadecane (◆, set D).

now transformed in a decrease of the parameter L/HLD for all oils. In case the observed correlation appears valid over wider ranges of SBA content and oil types it can be used as a predictive tool for the impact of the adding SBA or other co-solvents on micro-emulsion volumes and oil and water fractions ϕ_o once an L/HLD value is known.

3.3. Carbon number scans

The sample sets A, C and D can also be studied from a different point of view, where the alkane carbon number is scanned at fixed SBA contents of 1 wt%, 3 wt% and 5 wt%. Note that the salinity increases together with the alkane carbon number in order to maintain a type WIII microemulsion, and is further discussed below. In the left panel of Fig. 7 the carbon number dependence of the Teubner–Strey parameter d is plotted, showing an exponential decrease in d as the alkane carbon number increases. In the right panel of Fig. 7 the alkane carbon number dependence of the area per surfactant molecule A_s is plotted. Unlike the consistent trend observed for A_s as function of SBA content, no clear trend is seen here.

From Table 2 it can also be observed that for increasing alkane carbon number and equal SBA content the domain size parameters d and ξ_{TS} decrease. The interfaces become more folded for increasing alkane carbon number, which is an indication of a more flexible interface. This latter observation can be understood by the fact that the larger oil molecules have a smaller tendency to migrate in between the surfactant tails, implying a reduction of A_{SO} in Eq. (10), and therefore make the film less rigid. Alternatively one can argue that for longer carbon chains the terms A_{OO} and A_{SO} increase, but as Bourrel and Schechter [41] pointed out, A_{SO} increases linearly whereas A_{OO} increases quadratically with the alkane carbon number. The net effect results in a decrease of $A_{SO} - A_{OO}$, and consequently results in a decrease of the numerator in Eq. (10). Overall this means that with increasing the alkane carbon number, the net energies decrease, resulting in more flexible interfaces. It will be interesting to verify this hypothesis with neutron spin-echo measurements of the dynamics of the interfaces.

As discussed, the increase in carbon number results in a decrease in $A_{SO} - A_{OO}$, resulting in a dominance of the interactions on the water side of the interface. To restore the balance, a higher salinity is required (as can be seen from Table 1) to reduce the head group repulsion, and therefore making A_{HH} less negative which results in a decrease of the denominator. The magnitude of the interactions on both sides of the interface are now lowered while the Winsor R-ratio remains equal to unity, making the interface less rigid and thus more flexible which tends to reduce the water and oil domain sizes.

As can be seen from the left panel in Fig. 7, the structure size parameter d decreases exponentially as function of alkane carbon number. However, it is not expected that this trend continues indefinitely. Because of the double-tailed nature of the IOS surfactant, the tails have an effective chain length of 10–12 carbon atoms. For carbon numbers ≥15 it is expected that, due to their large size relative to the surfactant tails, the tail region is effectively fully depleted from oil molecules and no further impact on the surfactant film is expected.

In principle, the increase in carbon number is not expected to have

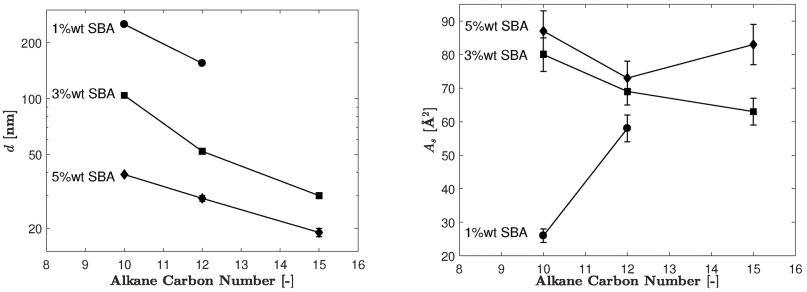

Fig. 7. Teubner-Strey parameter d in nm (left panel, semi-logarithmic scale) and the area per surfactant molecule A_s in Å^2 (right panel), each as function of Alkane Carbon Number, for an SBA content of 1 wt% (•), 3 wt% (■) and 5 wt% (♦). The lines are a guide to the eye.

any significant impact on the area per surfactant molecule A_s. The SBA molecules, by being located at the oil/water interface, mainly dictate the amount of (extra) space between the surfactant molecules as discussed previously. However, the oil molecules are only present in the tail region, and not in the water region or on the interface. Therefore, they will only affect the curvature of the interface instead of the space between the surfactant molecules. This is indeed observed in the right panel of Fig. 7 where no consistent trend with increasing carbon number is observed.

4. Summary and conclusions

In viscosity and core-flooding experiments on microemulsion systems by Humphry et al. [18], an unexpectedly high apparent viscosity was observed. A plausible explanation is that a fraction of the pore throats are similar or smaller in size as the structures the microemulsion consists of, thereby increasing the required pressure for the microemulsion to flow through the rock. Therefore, in this work a systematic study on the structure sizes of similar microemulsion systems was done. Using small angle neutron scattering techniques, the microemulsion structure sizes were quantified as function of salinity, co-solvent content, and alkane carbon number.

The salinity was varied in six different samples, where the full transition from a Winsor type WI→WIII→WII was measured. The differences in structure were identified with SESANS, where it was possible to distinguish dilute emulsified droplets from more concentrated droplets with a hard sphere interaction. The bicontinuous WIII type microemulsion consists of the largest structures found in this study. Furthermore, the difference in size between dilute emulsified droplets and bicontinuous structures is more than a factor of 3, and is larger than nearly 10% of the pore throats present in a reference rock sample. This indicates that this indeed causes an increased difficulty of flow in porous rock.

When increasing the SBA content, an exponential decrease is seen in the structure sizes of bicontinuous microemulsions. This trend is consistently observed throughout each sample set. The accompanying increase in area per surfactant molecule A_s matches with the theory that SBA molecules, located on the interface, repel the surfactant molecules. This increases the flexibility of the interface, allowing the system to fold to smaller structures, which is observed in the measurements. The inverse of the *HLD/L* parameter shows, within the ranges tested, a linear dependence on the SBA concentration. After normalization this relation is independent on oil type and salinity value.

The increase of the alkane carbon number has similar effects as is observed when increasing the co-solvent content. However, the mechanism responsible is not caused by an increase in space between surfactant molecules, but is rather caused by a decrease in interaction between the oil phase and the surfactant molecules. The net overall interactions are reduced making the interface more flexible. This effect, however, is thought to vanish when the oil molecules are significantly larger than the tails of the surfactant molecules. It will be interested to verify this hypothesis of the flexibility with neutron spin-echo measurements of the dynamics.

Crude oil generally consists of, among other compounds, alkanes with a wide variety of chain lengths, but with the foundation laid in this study it is a step forward towards understanding all effects together in such complex systems. This allows to predict their behaviour with HLD-NAC theory.

Acknowledgement

The authors thank Merit van der Lee from Shell Global Solutions for assisting in the preparation of the samples, and Stephen King and co-workers at the ISIS institute for assisting with the SANS measurements with the LARMOR instrument. This work benefited from the use of the SasView application, originally developed under NSF Award DMR-0520547. SasView also contains code developed with funding from the EU Horizon 2020 programme under the SINE2020 project Grant No 654000.

Appendix A. Derivation of $G_{TS}(z)$ for bicontinuous microemulsions

As mentioned in the text, the quantity that is measured with SESANS is the normalized Polarization $P(z)$,

$$P(z) = e^{\lambda^2 t(G(z)-G(0))} \tag{12}$$

where $G(z)$ is the projection of the (dimensionless) function $\gamma(r)$, which represents the autocorrelation of the density distribution function. The function $G(z)$ can be calculated by [26]

$$G(z) = 2\phi_o\phi_w\Delta\rho^2 \int_z^\infty \frac{\gamma(r)r}{\sqrt{r^2-z^2}}dr \tag{13}$$

which is multiplied by $\phi_o\phi_w\Delta\rho^2$ to obtain $G(z)$ in absolute units, which results in the dimension of $G(z)$ to be [m^{-3}]. Furthermore, in contrast to the definition of $G(z)$ by Andersson et al., here we choose not to normalize with $G(0)$. Eq. (13) is only valid if $\gamma(r)$ is isotropic, i.e. spherically symmetric.

$G(0)$ can in turn be calculated by

$$G(0) = 2\phi_o\phi_w\Delta\rho^2 \int_0^\infty \gamma(r)dr. \tag{14}$$

Teubner and Strey [28] derive their model for the SANS scattering intensity $I(Q)$ starting from the autocorrelation function of a density distribution $\gamma(r)$, which they postulate as

$$\gamma_{\mathrm{TS}}(r) = \frac{d}{2\pi r}\sin\left(\frac{2\pi r}{d}\right)\mathrm{e}^{-r/\xi_{\mathrm{TS}}} \tag{15}$$

where d is the mean domain repetition length, and ξ_{TS} the correlation length of the system. The function $\gamma_{TS}(r)$ is spherically symmetric, so Eq. (13) can be used to calculate $G_{TS}(z)$,

$$G_{\mathrm{TS}}(z) = \phi_o\phi_w\Delta\rho^2\frac{d}{\pi}\int_z^\infty \frac{\sin(\frac{2\pi r}{d})\mathrm{e}^{-r/\xi_{\mathrm{TS}}}}{\sqrt{r^2-z^2}}\mathrm{d}r. \tag{16}$$

Writing $\sin(\frac{2\pi r}{d})$ in terms of complex exponentials, the integral can be split into two integrals,

$$G_{\mathrm{TS}}(z) = \phi_o\phi_w\Delta\rho^2\frac{d}{2\pi\mathrm{i}}\left[\int_z^\infty \frac{\mathrm{e}^{\mathrm{ar}}}{\sqrt{r^2-z^2}}\mathrm{d}r - \int_z^\infty \frac{\mathrm{e}^{-\mathrm{br}}}{\sqrt{r^2-z^2}}\mathrm{d}r\right] \tag{17}$$

where $a = 2\pi\mathrm{i}/d - 1/\xi_{TS}$ and $b = 2\pi\mathrm{i}/d + 1/\xi_{TS}$, which are introduced for clarity. These integrals are alternative representations for the modified zeroth order Bessel function of the second kind [47], and thus can be rewritten as

$$G_{\mathrm{TS}}(z) = \phi_o\phi_w\Delta\rho^2\frac{d}{2\pi\mathrm{i}}[K_0(-\mathrm{az}) - K_0(\mathrm{bz})]. \tag{18}$$

The equivalence of Eqs. (17) and (18) is only valid, however, if the following conditions are satisfied, as provided by Wolfram|Alpha [48],

$$\mathrm{Re}(-a),\ \mathrm{Re}(\mathrm{b}) > 0 \tag{19}$$

$$\mathrm{Re}(z) > 0 \tag{20}$$

$$\mathrm{Im}(z) = 0 \tag{21}$$

The condition in Eq. (19) implies that it should hold that $1/\xi_{TS} > 0$, which is satisfied because a physical correlation length is never equal or less than zero. Furthermore, the condition in Eq. (20) implies that $G_{TS}(z)$ is only valid for $z > 0$, so $G(0)$ needs to be calculated with Eq (14). Finally, the condition in Eq. (21) is automatically satisfied since the spin-echo length z is real per definition.

The last step is then to calculate $G(0)$ by plugging in $\gamma_{TS}(r)$ in Eq. (14). It can be shown that

$$G_{\mathrm{TS}}(0) = \phi_o\phi_w\Delta\rho^2\frac{d}{\pi}\arctan\left(\frac{2\pi\xi_{\mathrm{TS}}}{d}\right) \tag{22}$$

as long as $\xi_{TS} > 0$, which is satisfied as described previously. The final result for projected autocorrelation function is then

$$G_{\mathrm{TS}}(z) - G_{\mathrm{TS}}(0) = \phi_o\phi_w\Delta\rho^2\frac{d}{2\pi}\left[\mathrm{i}[K_0(\mathrm{bz}) - K_0(-\mathrm{az})] - \left[2\arctan\left(\frac{2\pi\xi_{\mathrm{TS}}}{d}\right)\right]\right]. \tag{23}$$

Because the arguments $-az$ and bz of the Bessel functions are complex, the result is generally a complex number as well. However, $G(z) - G(0)$ is real, because the real parts of $K_0(bz)$ and $K_0(-az)$ are equal and are therefore canceled. The remaining imaginary parts are equal but opposite in sign, and is made real by the prefactor containing the imaginary number i. However, no mathematical proof for this is given yet, and has only been checked numerically.

Appendix B. Supplementary data

Supplementary data associated with this article can be found, in the online version, at https://doi.org/10.1016/j.colsurfa.2019.04.045.

References

[1] S. Slomkowski, J.V. Aleman, R.G. Gilbert, M. Hess, K. Horie, R.G. Jones, P. Kubisa, I. Meisel, W. Mormann, S. Penczek, R.F.T. Stepto, Terminology of polymers and polymerization processes in dispersed systems (IUPAC Recommendations 2011), Pure Appl. Chem. 83 (2011) 2229–2259.

[2] M.J. Lawrence, G.D. Rees, Microemulsion-based media as novel drug delivery systems, Adv. Drug Deliv. Rev. 45 (2000) 89–121.

[3] A. Bera, A. Mandal, Microemulsions: a novel approach to enhanced oil recovery: a review, J. Petrol. Explor. Technol. 5 (2015) 255–268.

[4] G.J. Hirasaki, C.A. Miller, M. Puerto, Recent Advances in Surfactant EOR, SPE, 2008, p. 115386.

[5] E. Goetheer, M. Vorstman, J. Keurentjes, Opportunities for process intensification using reverse micelles in liquid and supercritical carbon dioxide, Chem. Eng. Sci. 28 (2004) 121–191.

[6] B.K. Paul, S.P. Moulik, Microemulsions: an overview, J. Dispers. Sci. Technol. 18 (1997) 301–367.

[7] J.-L. Salager, R.E. Anton, D.A. Sabatini, J.H. Harwell, E.J. Acosta, L.I. Tolosa, Enhancing solubilization in microemulsions-state of the art and current trends, J. Surfact. Deterg. 8 (2005) 3–21.

[8] M.J. Rosen, H. Wang, P. Shen, Y. Zhu, Ultralow interfacial tension for enhanced oil recovery at very low surfactant concentrations, Langmuir 21 (2005) 3749–3756.

[9] C. Goddeeris, F. Cuppo, H. Reynaers, W. Bouwman, G.V. den Mooter, A study of the microstructure of a four-component nonionic microemulsion by cryo-TEM, NMR, SAXS, and SANS, Int. J. Pharm. 312 (2006) 187–195.

[10] N. Pal, S.D. Verma, M.K. Singh, S. Sen, Fluorescence correlation spectroscopy: an efficient tool for measuring size, size-distribution and polydispersity of microemulsion droplets in solution, Anal. Chem. 83 (2011) 7736–7744.

[11] O. Regev, S. Ezrahi, A. Aserin, N. Garti, E. Wachtel, E. Kaler, A. Khan, Y. Talmon, A study of the microstructure of a four-component nonionic microemulsion by cryo-TEM, NMR, SAXS, and SANS, Langmuir 12 (1996) 668–674.

[12] T. Sottmann, R. Strey, S. Chen, A small-angle neutron scattering study of nonionic surfactant molecules at the water–oil interface: area per molecule, microemulsion domain size, and rigidity, J. Chem. Phys. 106 (1997) 6483–6491.

[13] R. Angelico, A. Ceglie, G. Colafemmina, F. Delfine, U. Olsson, G. Palazzo, Phase behavior of the lecithin/water/isooctane and lecithin/water/decane systems, Langmuir 20 (2004) 619–631.

[14] C. Negin, S. Ali, Q. Xie, Most common surfactants employed in chemical enhanced oil recovery, Petroleum 3 (2017) 197–211.

[15] J.R. Barnes, H. Dirkzwager, J. Smit, J. Smit, A. On, R.C. Navarrete, B. Ellison, M.A. Buijse, Application of internal olefin sulfonates and other surfactants to EOR. Part 1: Structure–performance relationships for selection at different reservoir conditions, SPE Improved Oil Recovery Symposium (2010).

[16] P. Kumar, K.L. Mittal, Handbook of Microemulsion Science and Technology, CRC Press, 1999.

[17] D.L. Walker, C. Britton, D.H. Kim, S. Dufour, U. Weerasooriya, G.A. Pope, The Impact of Microemulsion Viscosity on Oil Recovery, SPE, 2012, p. 154275.

[18] K.J. Humphry, M. van der Lee, Microemulsion Rheology and Alkaline-surfactant-polymer Flooding, IOR, 2013.

[19] V. Sahni, R.M. Dean, C. Britton, D.H. Kim, U. Weerasooriya, G.A. Pope, The role of co-solvents and co-surfactants in making chemical floods robust, SPE Improved Oil Recovery Symposium (2010).

[20] L.Y. Chang, D.S. Lansakara-P, S.H. Jang, U.P. Weerasooriya, G.A. Pope, Co-solvent

partitioning and retention, SPE Improved Oil Recovery Conference (2016).
[21] J.-L. Salager, N. Marques, A. Graciaa, J. Lachaise, Partitioning of ethoxylated octylphenol surfactants in microemulsion–oil–water systems: influence of temperature and relation between partitioning coefficient and physicochemical formulation, Langmuir 16 (2000) 5534–5539.
[22] E. Acosta, E. Szekeres, D.A. Sabatini, J.H. Harwell, Net-average curvature model for solubilization and supersolubilization in surfactant microemulsions, Langmuir 19 (2003) 186–195.
[23] P. Winsor, Hydrotropy, solubilisation and related emulsification processes, Trans. Faradary Soc. 44 (1947) 376–398.
[24] S. Prévost, M. Gradzielski, T. Zemb, Self-assembly, phase behaviour and structural behaviour as observed by scattering for classical and non-classical microemulsions, Adv. Colloid Interface Sci. 247 (2017) 374–396.
[25] M.T. Rekveldt, J. Plomp, W.G. Bouwman, W.H. Kraan, S. Grigoriev, M. Blaauw, Spin-echo small angle neutron scattering in delft, Rev. Sci. Instrum. 76 (2005) 033901.
[26] R. Andersson, L.F. van Heijkamp, I.M. de Schepper, W.G. Bouwman, Analysis of spin-echo small-angle neutron scattering measurements, J. Appl. Crystallogr. 41 (2008) 868–885.
[27] S. Moulik, B. Paul, Structure, dynamics and transport properties of microemulsions, Adv. Colloid Interface Sci. 78 (1998) 99–195.
[28] M. Teubner, R. Strey, Origin of the scattering peak in microemulsions, J. Chem. Phys. 87 (1987) 3195–3200.
[29] A. Martino, E. Kaler, Phase behavior and microstructure of nonaqueous microemulsions, Langmuir 11 (1995) 779–784.
[30] H. Walderhaug, K.D. Knudsen, Microstructures in aqueous solutions of a polyoxyethylene trisiloxane surfactant and a cosurfactant studied by SANS and NMR self-diffusion, Langmuir 24 (2008) 10640–10652.
[31] P. Heunemann, S. Prevost, I. Grillo, C.M. Marino, J. Meyer, M. Gradzielski, Formation and structure of slightly anionically charged nanoemulsions obtained by the phase inversion concentration (PIC) method, Soft Matter 7 (2011) 5697–5710.
[32] S.-H. Chen, S.-M. Choi, Measurement and interpretation of curvatures of the oil–water interface in isometric bicontinuous microemulsions, J. Appl. Crystallogr. 30 (1997) 755–760.
[33] S. Choi, S. Chen, T. Sottmann, R. Strey, The existence of three length scales and their relation to the interfacial curvatures in bicontinuous microemulsions, Physica A 304 (2002) 755–760.
[34] N. Freiberger, C. Moitzi, L. de Campo, O. Glatter, An attempt to detect bicontinuity from SANS data, J. Colloid Interface Sci. 312 (2007) 59–67.
[35] T. Krouglov, I.M. de Schepper, W.G. Bouwman, M.T. Rekveldt, Real-space interpretation of spin-echo small-angle neutron scattering, J. Appl. Crystallogr. 36 (2003) 117–124.
[36] J.K. Percus, G.J. Yevick, Analysis of classical statistical mechanics by means of collective coordinates, Phys. Rev. 110 (1958) 1–13.
[37] M. Doucet, et al., SasView Version 4.1. Zenodo, https://zenodo.org/record/438138#.WSWDeGjyjcs.
[38] G. Porod, O. Glatter, O. Kratky (Eds.), Small Angle X-ray Scattering, Academic, New York, 1982.
[39] M. Bourrel, R. Schechter, Microemulsions and Related Systems, Marcel Dekker, New York, 2006.
[40] J.G. Fraaije, K. Tandon, S. Jain, J.-W. Handgraaf, M. Buijse, Method of moments for computational microemulsion analysis and prediction in tertiary oil recovery, Langmuir 29 (2013) 2136–2151.
[41] M. Bourrel, R. Schechter, Microemulsions and Related Systems: Formulations, Solvency and Physical Properties, Editions Technips, 2010.
[42] M. Kotlarchyk, S. Chen, J. Huang, Temperature dependence of size and polydispersity in a three-component microemulsion by small-angle neutron scattering, J. Phys. Chem. 86 (1982) 3273–3276.
[43] L. Arleth, J.S. Pedersen, Droplet polydispersity and shape fluctuations in AOT microemulsions studied by contrast variation small-angle neutron scattering, Phys. Rev. E 63 (2001) 061406.
[44] O. Uca, W.G. Bouwman, M.T. Rekveldt, Model calculations for the spin-echo small-angle neutron-scattering correlation function, J. Appl. Crystallogr. 36 (2003) 109–116.
[45] J. Schelten, W. Schmatz, Multiple-scattering treatment for small-angle scattering problems, J. Appl. Crystallogr. 13 (1980) 385–390.
[46] S.K. Kiran, E.J. Acosta, Predicting the morphology and viscosity of microemulsions using the HLD-NAC model, Ind. Eng. Chem. Res. 49 (2010) 3424–3432.
[47] NIST, Digital Library of Mathematical Functions. http://dlmf.nist.gov/10.32#E8, Release 1.0.15 of 2017-06-01, consulted on June 13, 2017.
[48] Wolfram|Alpha, Wolfram Alpha LLC. http://www.wolframalpha.com/input/?t=crmtb01&f=ob&i=integrate+exp(a*r)%2Fsqrt(r%5E2-z%5E2)dr;+z%3Cr%3Cinf, consulted on June 13, 2017.